Ultrasonics Sonochemistry 79 (2021) 105767

Contents lists available at ScienceDirect

Ultrasonics Sonochemistry

journal homepage: www.elsevier.com/locate/ultson

Mesoporous onion-like carbon nanostructures from natural oil for high-performance supercapacitor and electrochemical sensing applications: Insights into the post-synthesis sonochemical treatment on the electrochemical performance

Athiyanam Venkatesan Ramya, Riya Thomas, Manoj Balachandran *

Materials Science Research Laboratory, Department of Physics and Electronics, CHRIST (Deemed to be University), Bengaluru 560029, Karnataka, India

ARTICLE INFO

Keywords:
Onion-like carbon
Sonochemical parameters
Binder-free electrode
Supercapacitor
Electrochemical sensor
Methylene blue

ABSTRACT

Although onion-like carbon nanostructures (OLCs) are attractive materials for energy storage, their commercialization is hampered by the absence of a simple, cost-effective, large-scale synthesis route and binder-free electrode processing. The present study employs a scalable and straightforward technique to fabricate sonochemically tailored OLCs-based high-performance supercapacitor electrode material. An enhanced supercapacitive performance was demonstrated by the OLCs when sonicated in DMF at 60 °C for 15 min, with a specific capacitance of 647 F/g, capacitance retention of 97% for 5000 cycles, and a charge transfer resistance of 3 Ω. Furthermore, the OLCs were employed in the electrochemical quantification of methylene blue, a potential COVID-19 drug. The sensor demonstrated excellent analytical characteristics, including a linear range of 100 pM to 1000 pM, an ultralow sensitivity of 64.23 pM, and a high selectivity. When used to identify and quantify methylene blue in its pharmaceutical formulation, the sensor demonstrated excellent reproducibility, high stability, and satisfactory recovery.

1. Introduction

With the depletion of energy resources and ongoing climate menace, the global supercapacitor market is developing alternative energy storage equipment that imparts the least environmental damage. The foremost priorities of high performance and sustainability have encouraged readily biodegradable carbon to fabricate supercapacitors. Carbon materials' morphology and porous structure optimize the charge storage mechanism via double layer formation [1]. Among the members of the carbon family, onion-like carbon (OLCs), also referred to as carbon nano-onions (CNOs), is an important allotrope that is utilized extensively for high-performance supercapacitors. Compared to traditional carbonaceous materials like activated carbon and carbon nanotubes (CNTs), OLCs have a well-developed porous structure, low density, and enhanced stability envisioned as an excellent electrode material. The concentric graphitic multi-shells of OLCs enable facile ion accessibility and high electronic conduction via its spherical geometric surface, allowing fast charge-discharge rates [2].

Since 1992, with the first report on onion-like fullerenes, several strategies have been developed to synthesize OLCs towards supercapacitor applications, including laser-assisted combustion [3], underwater arc-discharge [4], and vacuum annealing [5]. However, these techniques require high energy, activation processes, sophisticated designs, and their yield is either low or allied with redundant by-products. Despite the innate characteristics, the practical applicability of OLCs intended for electrochemical performance is significantly obstructed due to the lack of convenient and cost-effective preparation methods. Therefore, a simple, economical, and scalable synthesis technique employing a sustainable carbon precursor must be identified to generate porous graphitized OLCs.

Upon utilizing carbon materials, the cost of supercapacitors relies on the choice of economically viable precursors, scalable synthesis procedures, and facile electrode processing techniques. The nanosize of the OLCs instigate the need for an appropriate binder for their usage as electrodes, typically 10 mass% PTFE (Polytetrafluoroethylene) [6]. Nonetheless, the main consequence is the increased resistivity and declined cyclic stability of the electrode material due to the blockage of electroactive sites by the binder [7]. Hence the development of binder-

* Corresponding author.
E-mail address: manoj.b@christuniversity.in (M. Balachandran).

https://doi.org/10.1016/j.ultsonch.2021.105767
Received 17 September 2020; Received in revised form 13 September 2021; Accepted 20 September 2021
Available online 24 September 2021

less carbon electrodes is a subject of intense research for enhanced performance, reduced cost, and facile electrode processing.

Apart from the geometrical dependence on the design of carbon nanomaterials for supercapacitor performance, the impact of chemical attributes is also a crucial factor for the choice. The oxygen functionalities on the carbon surface increase the electrode's wettability and augment the capacitive performance via redox reactions contributing to pseudocapacitive effects [8]. However, not all the surface functional groups benefit the supercapacitor performance of electrode material. For example, phenolic hydroxyl groups offer large capacitance compared to carboxyl groups [9]. Consequently, a systematic investigation is essential to understand the effect of the oxygen functional groups on the capacitive properties of the carbon-based electrochemical supercapacitor.

The other critical aspect of fully exploiting the advantages of OLCs lies in the synthesis history. Modifications in synthesis conditions alter the microtexture, chemical nature, and extent of functionalization of the OLCs but preserve their concentric graphitic shells [10]. It has been reported that the post-synthetic treatment on the preformed OLCs has a significant impact on its electrochemical properties [11]. The main strategies adopted for this purpose include i) heteroatom doping and ii) oxidation or reduction processes [12,13]. However, there are not many reports on the electrical double-layer properties and charge storage mechanisms of ultrasound-treated OLCs. It is known that the physiochemical effects of cavitation are strongly dependent on sonochemical parameters, including solvent properties (vapor pressure, viscosity, density), the temperature of the sonicated solution, duration of sonication, and ultrasonic intensity [14]. Therefore, it is critical to rationalize these parameters for the optimum energy storage ability of the OLCs. To advance the study further, it is essential to explore other possible electrochemical applications of the OLCs.

The devastation wreaked by the SARS-CoV-2 virus as the COVID-19 pandemic is witnessed globally, evidenced by the ever-growing statistics. Worldwide, various drugs or combinations of drugs are being evaluated to identify effective and affordable antiviral medications with fewer side effects. In this context, several researchers have proposed methylene blue (MB), a traditional therapeutic agent used in medicine, as a promising drug for preventing and treating COVID-19 due to its antiviral activity against SARS-CoV-2 [15,16]. Clinical trials with MB on COVID-19 patients demonstrated increased oxygen saturation and respiratory rate, resulting in a shorter hospital stay and decreased mortality [17]. However, a meticulous dosage is necessary for MB administration (oral/intravenous) to prevent toxic manifestations.

Quality control (QC) is a critical component of pharmaceutical research because it ensures the drug's purity, safety, and effectiveness. As the first step in drug quality control, qualitative and quantitative analytical methods are typically employed to evaluate the stability of pharmaceuticals [18]. Electrochemical techniques have grown in popularity over the last few years as an alternative to other analytical methods used in the quality control of drugs [19]. The present study demonstrates the potential utility of OLCs as electrode materials for the electrochemical quantification of MB.

The current study aims to develop ultrasound-modified OLCs as a binder-free electrode material with optimized supercapacitive performance and ultrasensitive electrochemical detection. The supercapacitive behavior of cavitation-induced modifications on OLCs derived from paraffin oil is proposed for the first time in this report. In addition, the electrochemical quantification of MB by sonochemically-treated OLCs is reported herein for the first time. Aside from the lack of similar studies on OLCs, the novelty of our approach stems from the exceptional analytical performance of the developed sensor towards quantifying MB drug, which is considered the 'rescue magic bullet' against COVID-19.

2. Experimental section

2.1. Materials

Chemicals and solvents of analytical grade were procured and utilized without any further purification. Deionized and doubly distilled water was used for all the relevant studies.

2.2. Instrumentation

Transmission Electron Micrographs were recorded by JEM-2100 (JOEL) High-Resolution Transmission Electron Microscope (HRTEM). The Fourier Transform Infrared (FTIR) spectra were captured with a 4 cm^{-1} spectral resolution using Thermo Nicolet-Avtar 370 spectrometer. Raman spectral measurements were performed on a Horiba LabRAM HR spectrometer (Incident wavelength – 514.5 nm). The chemical composition of the samples was analyzed by Omicron ESCA probe X-ray Photoelectron Spectroscope (XPS) employing polychromatic Mg Kα X rays ($h\nu = 1253.6$ eV). The BET-specific surface area (SSA) and pore size distribution analyses were performed at liquid nitrogen temperature on the Quanta Chrome Nova-1000 surface analyzer. The Voltammetric measurements were done in a 3-electrode cell electrochemical workstation model CH 660E.

2.3. Preparation of as-synthesized and sonicated OLCs

Paraffin oil was purchased from a pharmacy in Bangalore, India. A clean and dry cotton wick was immersed in a corked glass bottle filled with paraffin oil. The free end of the wick was ignited, and the oil was burnt in a stable wind-free atmosphere with the aid of a glass chimney. The carbonaceous soot was captured using an inverted ceramic dish clipped at 3 cm above the flame. The as-synthesized carbon structures (a-OLCs) were washed with ethanol and collected via centrifugation, followed by evaporation. To prepare ultrasonicated OLCs, (s-OLCs), 2 g of a-OLCs was dispersed in distilled water (30 mL) and ultrasonicated for 60 min in a bath ultrasonicator (30 kHz) and then evaporated until dry. Different sonication parameters, including solvent, time, and temperature, were applied to prepare optimized OLCs (o-OLCs) with enhanced energy storage abilities. The a-OLCs were dispersed in various solvents like acetonitrile, DMF, DMSO, ethanol, H_2O_2, and NMP and sonicated at 60 °C for 30 min. To understand the effect of time, a-OLCs was sonicated in DMF at 60° C for 10, 15, 20, 25, and 30 min. Finally, with the optimized solvent (DMF) and time (15 min), a-OLCs was sonicated at temperatures RT, 40 °C, 60 °C, and 80 °C. a-OLCs sonicated at 60 °C for 15 min in DMF was coded o-OLCs.

2.4. Electrochemical measurements

The electrochemical measurements were performed with glassy carbon as the working electrode, saturated calomel electrode, and Platinum wire as reference and counter electrode, respectively, in 1 M H_2SO_4 as the electrolyte. The individual electrochemical response of pristine and sonicated OLCs was analyzed using cyclic voltammetry and galvanostatic charge–discharge techniques. The alternating-current impedance was conducted for a 5 mV signal in the frequency range of 1 Hz to 100 kHz.

2.5. Electrochemical quantification of MB at modified GCE

o-OLCs modified GCE prepared in section 2.3 was used as the working electrode for detecting MB in combination with Platinum wire and saturated calomel as counter and reference electrodes, respectively. Analytical parameters like the electrolyte, type of electrode, and the electro-analytical mode were optimized by studying the methylene blue (MB) sensing efficiency of the o-OLCs, aiming for the best performance. The electro-sensing of MB at o-OLCs was performed in 0.1 M HCl

(electrolyte) by square wave voltammetry. The reproducibility and repeatability of the o-OLCs were tested in 500 pM MB solution. For interference studies, each interfering species was mixed in 1:1 vol ratio of 500 pM MB solution. For real-sample analysis, three different concentrations of MB injection were prepared. All the sensing experiments were repeated thrice to ensure reproducibility.

3. Results and discussion

3.1. Morphological, compositional, and textural characterization of the OLCs

The surface morphology of the as-synthesized and sonicated carbon nanostructures is elucidated by TEM (Fig. 1(a–f)). Several interconnected, nearly spherical concentric multi-shelled onion-like nanostructures are noticed in the as-synthesized sample (Fig. 1(a–c)), mimicking the characteristic feature of OLCs. The as-synthesized nanostructures exhibit an average particle size of 41 ± 0.32 nm (Fig. S1(a)). Upon sonication, the nanostructures retain their onion-like structure with a marginal decrease in the average particle size to 34.41 ± 0.23 nm (Fig. S1(b)).

The structural investigation of the as-prepared and the sonicated OLCs were carried out by Raman spectral analysis. The spectra reveal two dominant peaks assigned to D and G bands for the as-prepared OLCs at 1345 cm^{-1} and 1588 cm^{-1} (Fig. 2(a)) and the sonicated OLCs at 1352 cm^{-1} and 1593 cm^{-1} (Fig. 2(b)), respectively. The G band, generally positioned at 1582 cm^{-1} for graphite, is found to be red-shifted for the as-prepared OLCs due to the tensile strain created by the curved geometry of the OLCs shells [20]. Upon sonication, these bands are further shifted with respect to that of as-prepared OLCs, suggesting a change in the lattice structure of the sonicated OLCs. The intense and broad D-band appears primarily due to the heptagonal and pentagonal rings which produce the curved shells. The D-band is highly sensitive to structural disorder and defects and is also caused by the amorphous/sp^3 carbon, surface functional groups, disrupted sp^2 hybridized carbon

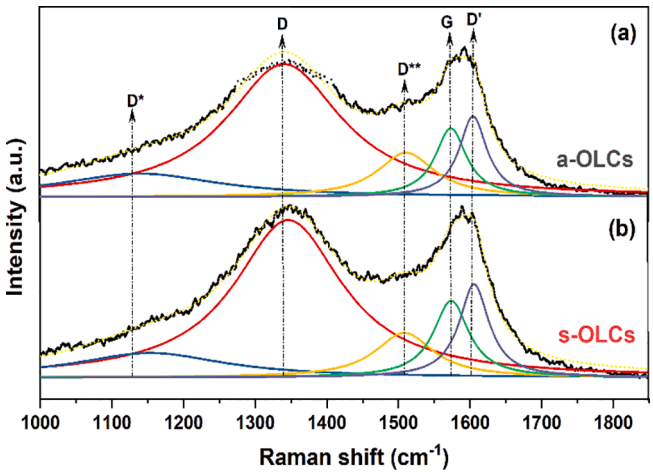

Fig. 2. Deconvoluted first-order Raman spectra of (a) as-synthesized and (b) sonicated OLCs. The solid black lines represent the original experimental spectra, and the yellow dotted lines represent the sum of the deconvoluted peaks. (For interpretation of the references to colour in this figure legend, the reader is referred to the web version of this article.)

network, intercalated C and H atoms, vacancies, dangling bonds, foreign atoms, etc. in the OLCs [21–23]. The ratio of the intensity of D band to G band is a significant parameter to determine the disorder degree in carbon materials. The I_D/I_G ratio of as-synthesized OLCs is computed to be 0.94, implying a moderate degree of graphitization, comparable to the OLCs reported previously [20]. Upon sonication, the I_D/I_G ratio increases to 1.12, signifying an increase in the density of defects. Other authors have observed a similar trend for different carbon structures [24,25].

The deconvoluted first-order Raman spectra of the OLCs are shown in Fig. 2, fitted with five peak functions accredited to D, G, D′, D**, and D* bands. Broadening of G band is detected as an increase in its FWHM

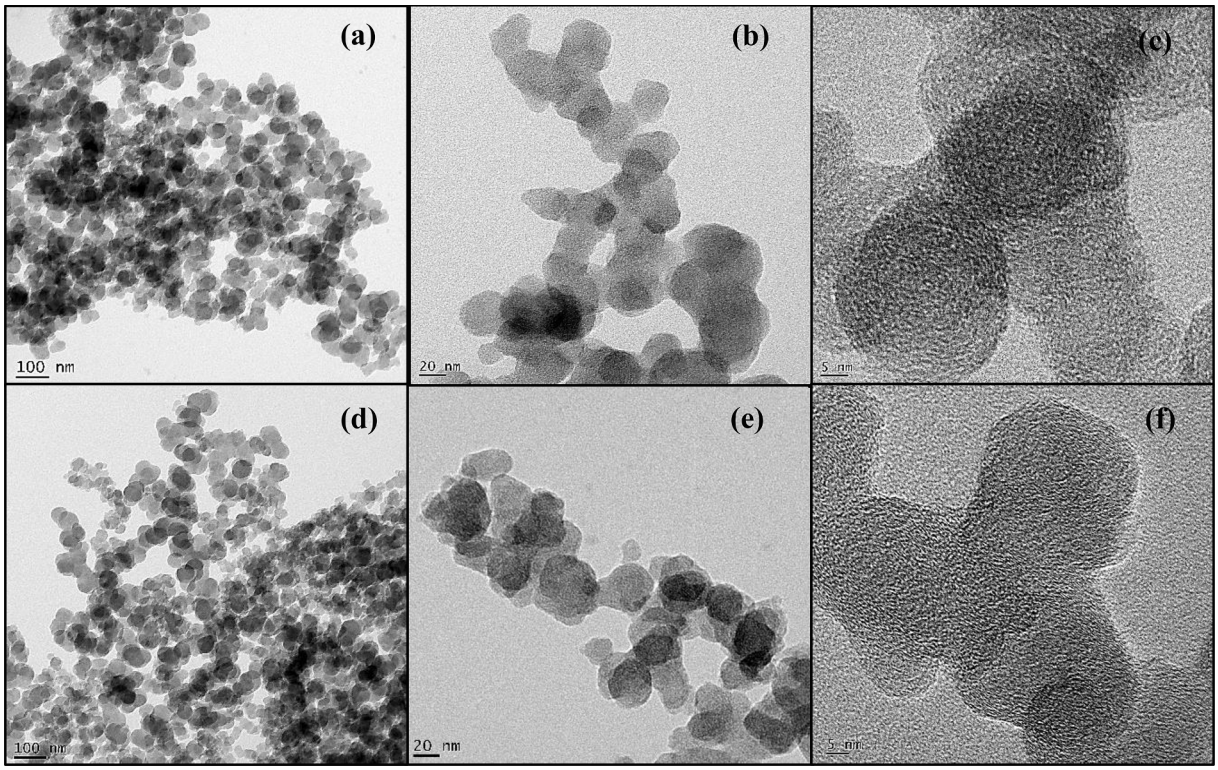

Fig. 1. HRTEM images of (a–c) as-synthesized and (d–f) sonicated nanocarbon structures exhibiting onion-like morphology.

from 53.24 cm^{-1} to 60.19 cm^{-1}, after sonication, which can be ascribed to the increase in the defects and breaking of the conjugated π system in the OLCs. D′ band is designated to the vibration mode warranting structural defects on the surface of the OLCs [26,27]. The intensities of D and D′ bands correspond to the type and density of defects. Upon sonication, an increase in the intensity of the D and D′ bands is observed in the OLCs, implying an increase in the concentration of defects. The occurrence of D** band confirms the presence of amorphous carbon and different functional moieties in OLCs [28–30]. D* band, the lower energy shoulder of the D band is due to the sp^2-sp^3 disordered graphitic lattice of the OLCs. The positions of the intensity maxima of the D* and D** bands usually rely on oxygen concentration. Diaz et al. have reported that the D* band shifts to a shorter wavelength on increasing the oxygen content, whereas the D** band shifts to farther wavelengths [31]. In the current study, the D* and D** bands of the as-prepared OLCs shift from 1132 cm^{-1} to 1151 cm^{-1} and from 1511 cm^{-1} to 1506 cm^{-1} upon sonication. This implies that the ultrasonic treatment has partially removed certain oxygen functional groups from the as-prepared OLCs. The sonicated OLCs show a loss in the concentration of certain oxygen species and an increase in the density of defects and disorder.

The nature of functional groups in the as-synthesized and the sonicated OLCs were examined by FTIR analysis (Fig. 3). For as-synthesized OLCs, the broad peak centered at ~3425 cm^{-1} is associated with the stretching vibrations of alcohols, carboxylic groups, and adsorbed water (ν_{O-H}) [32,33]. The peaks noticed at 3708 cm^{-1}, and 3780 cm^{-1} are due to free/unassociated OH groups. The peak discerned at 1592 cm^{-1} is a consequence of the conjugated stretching mode of sp^2 carbon ($\nu_{C=C}$) and carbonyl groups ($\nu_{C=O}$) and bending mode of hydroxyl groups (δ_{O-H}). The broad peak at 1184 cm^{-1} arises from the stretching vibration of carboxyl, phenol, and epoxy groups (ν_{C-O}) [23,34]. The oxygen moieties on the a-OLCs emerge during the open-air synthesis. They render the sample high dispersibility and hydrophilicity.

In the sonicated OLCs, a noticeable decline in the intensity and the FWHM of the –OH stretching mode (ν_{O-H}) indicates partial removal of the –OH functional groups. Additionally, the sharp, intense peak observed at 3785 cm^{-1} specifies the existence of larger unbonded OH groups generated during the sonication process. The decrease in intensity of the peak at 1584 cm^{-1} implies an increase in defects accompanied by the reduction in –OH species. The decrease in the FWHM of the peak at 1156 cm^{-1} indicates partial elimination of C-O groups. Compton et al. have reported a decline in the number of carboxyl groups in graphene oxide upon sonication [35]. The FTIR spectroscopic analysis results suggest that the sonochemical treatment has decreased the oxygen functional groups.

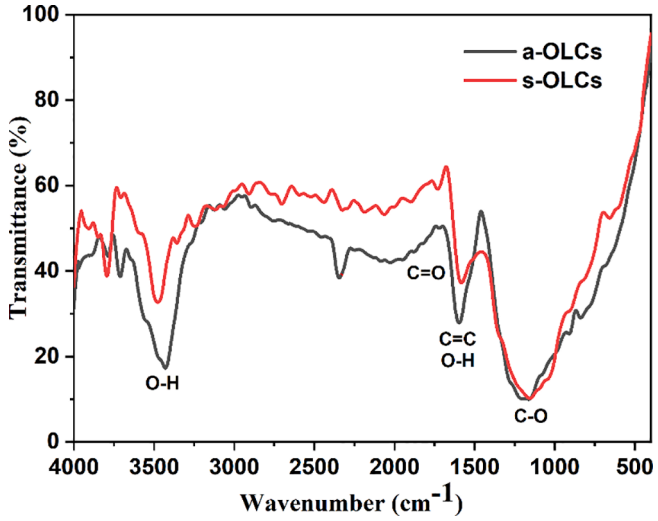

Fig. 3. FTIR spectra of as-synthesized and sonicated OLCs.

The X-ray photoelectron spectroscopy (XPS) survey scan (Fig. S2 (a) and (b)) revealed the presence of graphitic C1s peak at around 284 eV and oxygenous O1s peak at about 533 eV for both the as-prepared and the sonicated OLCs. The C/O ratio decreased from 1.87 in the as-prepared OLCs to 1.37 in the sonicated OLCs, disclosing the elimination of some oxygeneous groups upon sonochemical treatment. The C1s XPS spectra of the as-prepared (Fig. 4 (a)) and sonicated OLCs (Fig. 4 (b)) were deconvoluted into four components. In both the samples, the prominent peak at ~284.5 eV is attributed to graphitic sp^2 carbon, and the peak at ~285.4 eV corresponds to disordered sp^3 carbon fraction in the OLCs. The peaks at ~286.5 eV and ~288.8 eV are attributed to oxygen functionalities, namely C–O (such as hydroxyl, phenol, epoxide) and C═O (such as carbonyl, carboxyl) [36]. An appreciable decrease in the sp^2 carbon and increase in the sp^3 carbon component is witnessed, revealed by the decrease in the Csp^2/Csp^3 ratio from 5.1 in as-prepared OLCs to 2.6 in sonicated OLCs, confirming the increase in defects generated by ultrasonication treatment.

The component fractions of the samples computed from the area under the fitted peaks are displayed in Fig. 5. Noticeable loss of C–O and C═O oxygen functional groups is observed after sonication. The hydroxyl and epoxide groups are regarded to be relatively facile for removal by ultrasonication [37]. A similar loss in the oxygen functional groups upon sonication was observed by Nam et al. [38]. Goncalves et al. has reported that ultrasonication causes a decline or transformation of the C–O–C/C–OH groups into C–H/C═O moieties, leading to an increased C/O ratio [39].

Nitrogen sorption measurements were carried out to deduce the specific surface area (SSA) and pore size distribution (PSD) of the as-synthesized and the sonicated OLC samples (Refer Table S1 for parameters). The OLCs portray type II isotherms with H3 hysteresis loop, typical to structures with a strong tendency to form agglomerates (Fig. 6 (a)). The multipoint BET measurement reveals the SSA of the as-synthesized and the sonicated OLCs to be 85 m^2/g and 101 m^2/g, respectively. Fig. 6(b) displays the PSD curves of the OLCs obtained from the N_2 desorption experiment (BJH method). The as-synthesized and the sonicated OLCs exhibit an average pore width of 2.324 nm and 2.152 nm, respectively.

3.2. Electrochemical performance analysis of the OLCs

The capacitive performance of the as-synthesized OLCs and the impact of cavitation-assisted ultrasound treatment on the capacitive behavior of the a-OLCs were investigated using the cyclic voltammetry (CV) technique. The electrochemical performance of a-OLCs and s-OLCs were assessed at different scan rates from 10 mV/s to 1000 mV/s, and the representative cyclic voltammograms are portrayed in Fig. 7. The quasi-rectangular CV curves and the small redox peaks of a-OLCs (Fig. 7 (a)) advocate the synergistic contribution of both electric double layer capacitance (EDLC) and pseudocapacitance. The observed current peaks denote the cathodic and anodic reactions of the surface oxygen groups in the a-OLCs [40]. The symmetric peak shift of these redox peaks over the entire scan range signifies the reversible charge-discharge mechanism in a-OLCs [41]. However, in s-OLCs (Fig. 7(b)), the redox peaks are not prominent because sonication resulted in reduced surface oxygen moieties and led to fewer oxidation/reduction processes.

The mechanism involved in the pseudocapacitance of both the samples can be interpreted in two ways: i) carbon surface enriched with oxygen functional groups ii) carbon surface with comparatively lesser oxygen functional groups. An oxygen-rich electrode material can easily initiate redox reactions with H^+ ions in an acidic electrolyte solution. These redox-mediated reactions generate an adsorption interface with the surface of the electrode that is favorable for electron transfer [42]. These reactions are referred to in the following formulas:

$$> C_xO + H^+ => C_xO//H^+ \text{ (Adsorption of } H^+) \quad (1)$$

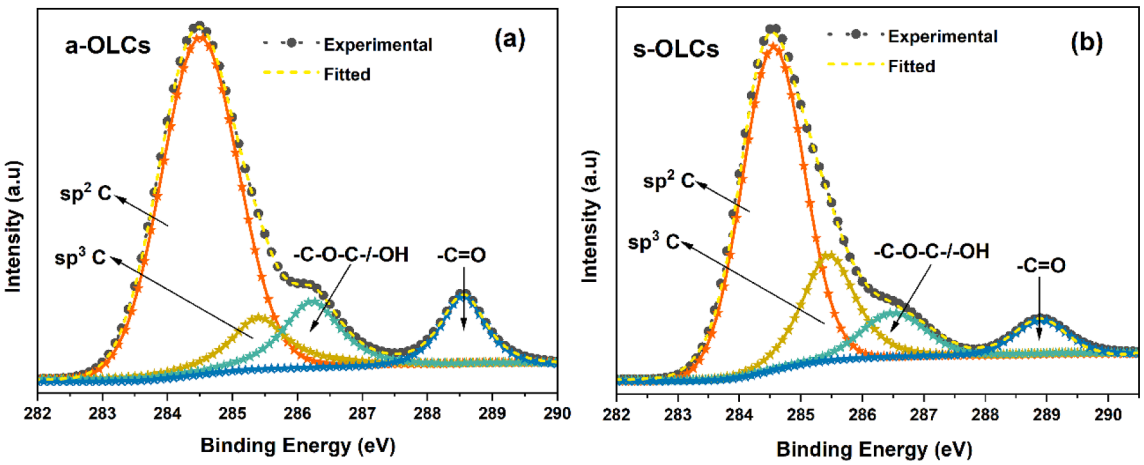

Fig. 4. High-Resolution C1s XPS spectra of (a) as-synthesized and (b) sonicated OLCs fitted by Voigt line shapes after applying Shirley background.

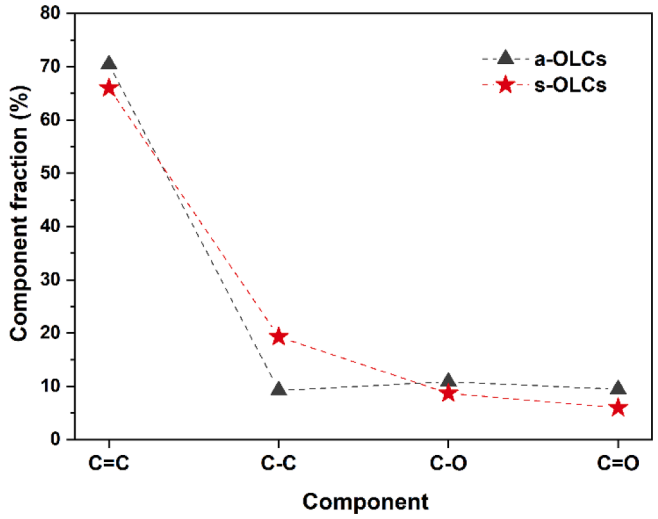

Fig. 5. The component fraction of different functional moieties of as-synthesized and sonicated OLCs.

where > and // represent carbon surface and adsorption interface, respectively.

$$> C_xO + H^+ + e^- => C_xOH \text{ (Electron transfer)} \quad (2)$$

In the case of a-OLCs modified electrode, H_3O^+ in the H_2SO_4 electrolyte solution interacts with the hydroxyl group of the OLCs inducing a redox reaction. In this process the hydroxyl group loses an electron, expressed as:

$$> C_xO + H^+ + H_2O + e^- => C_xOH\ (H_2O) \quad (3)$$

The sonicated sample (s-OLCs) does not include this redox reaction due to the reduced number of surface oxygen moieties. In this instance, where the oxygen group cannot ensue the oxidation/reduction processes, the configuration of the Helmholtz layer is more permissible. Under the applied electric field, the polarised carbon surface forms the inner Helmholtz layer, and H_3O^+ forms the outer Helmholtz layer around the electrode surface [43].

To understand the electrochemical environment of the samples, the variation in the peak current with applied scan rate is studied and is displayed in Fig. 8 (a) and (b). The slope of the linear plot of log *v* versus log *i* provides the value of coefficient b, which governs the rate-limiting step of the electrochemical reaction. The value b = 1 demonstrates a pseudocapacitive material involving surface redox-mediated reactions, and value b = 0.5 represents a battery-type material owning diffusion-controlled processes [44]. The b-value is ~1 for both anodic and cathodic peak currents of a-OLCs, suggesting surface-controlled fast faradic reactions. The s-OLCs exhibit a decrease in the slope value of b to 0.5, indicating the slow semi-infinite linear diffusion. This rate limitation of the s-OLCs is mainly due to the increase in the ohmic contribution of the active material resulting from the destruction of oxygen moieties upon sonication. The oxygen functionalities in a-OLCs attached to the carbon shells can lead to increased wettability of the electrode and hence augment conductivity [45]. It is noteworthy that reducing in-

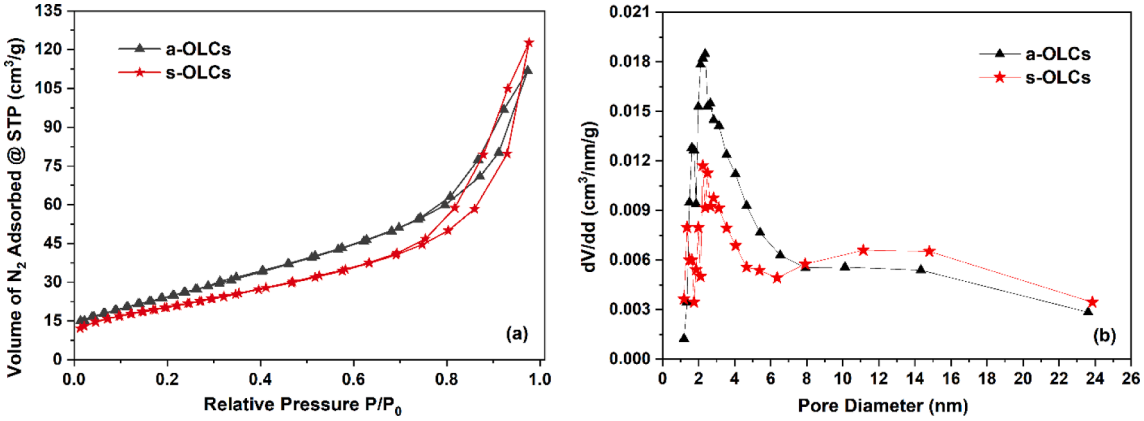

Fig. 6. (a) N_2 adsorption/desorption isotherms and (b) Pore size distribution of as-synthesized and sonicated OLCs.

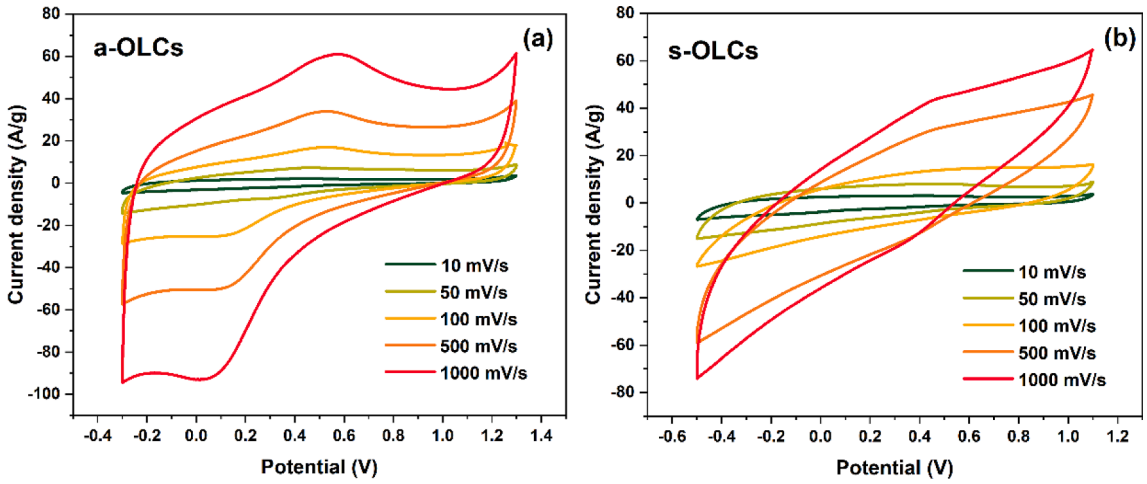

Fig. 7. CV curves of electrodes modified with (a) as-synthesized OLCs and (b) sonicated OLCs at different scan rates.

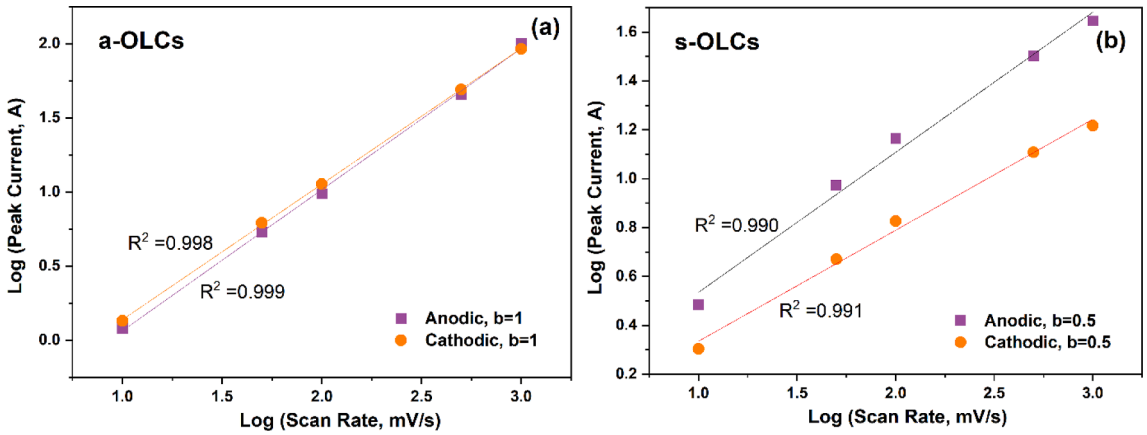

Fig. 8. A plot of log (peak current) vs. log (scan rate) for (a) as-synthesized OLCs and (b) sonicated OLCs.

plane oxygen functional groups via ultrasonic treatment alters the pseudocapacitive-type into a battery-type electrode.

The rate performance of as-synthesized OLCs is presented in Fig. 9 (a). The retarding specific capacitance at higher scan rates can be accredited to the quicker ion motions obstructing ions' dispersion into the electrode material's pores. Although, at lower scan rates, the diffused ions get sufficient time to completely access the inner space of the nanomaterial [34]. Among the two samples, a-OLCs exhibit a better capacitive behavior with a calculated specific capacitance of 259 F/g, significantly higher than that of s-OLCs (157 F/g). The comparatively higher oxygen content in a-OLCs elevated its capacitive performance owing to the pseudocapacitance arising from the redox reactions. But the variation of specific capacitance with an increase in scan rate was minor for s-OLCs compared to a-OLCs, suggesting its higher rate capability. This is because the surface functionalities of s-OLCs adversely affected the in and out motion of the electrolyte ions [46]. The cyclic stability of the samples was tested by galvanostatic charge-discharge (GCD) at 5 A/g, and the results are displayed in Fig. 9 (b). The s-OLCs and a-OLCs have retained 95% and 84% of the initial capacitance after 5000 cycles, respectively, even though the onion-like carbon morphology constitutes a reasonable charge propagation ability in both the samples, the comparatively higher amount of oxygen moieties in the case of a-OLCs results in decreased stability [47].

The charge transfer mechanisms involved in as-synthesized and sonicated OLCs were evaluated by the impedance spectroscopic technique. The Nyquist plot drawn with the impedance data consists of three different frequency regions: i) high-frequency region with a semicircle that corresponds to charge-transfer process at the electrode-electrolyte interface; ii) a 45° Warburg zone in intermediate frequency relates to diffusion resistance; and iii) vertical straight line (~90°) in low-frequency region that responds to an ideal capacitive behavior [48]. As seen in Fig. 9(c) and (d), the narrow semicircle detectable in the high-frequency range is due to the appreciable electrical conductivity endorsed by the OLCs. It is also observed that the vertical line in the low-frequency region of a-OLCs approaches 90° in comparison to the s-OLCs. This sharp increase at low frequency clearly indicates the enhanced capacitive behavior of a-OLCs [49].

The experimental data are fitted utilizing a fitting algorithm to propose the equivalent circuit model that best describes the electrochemical behavior (inset of Fig. 9(c) and (d)). The equivalent circuit model consists of two constant phase elements (CPE), 3 resistors (R_s, R_{ct}, R_1), and a Warburg element (W1). An additional contribution from the Warburg element in a-OLCs represents increased ionic diffusion impedance, which might be explained in terms of steric hindrance from surface oxygen moieties [50]. The electrolyte resistance, R_s for a-OLCs, and s-OLCs are calculated to be 4.67 Ω and 4.34 Ω, respectively. Similarly, the obtained charge-transfer resistance, R_{ct}, is 3.48 Ω for a-OLCs and 13.1 Ω for s-OLCs. The adsorption-desorption resistance is found to be 650 Ω and 130 Ω for a-OLCs and s-OLCs, respectively. The a-OLCs possess plenty of oxygen functional groups that contribute to Warburg impedance and higher electrolyte resistance. At the same time, these oxygen moieties improved the hydrophilicity of the sample at the electrode surface, facilitating reduced charge transfer resistance. The above observations reveal the equivalent contribution of the electrode

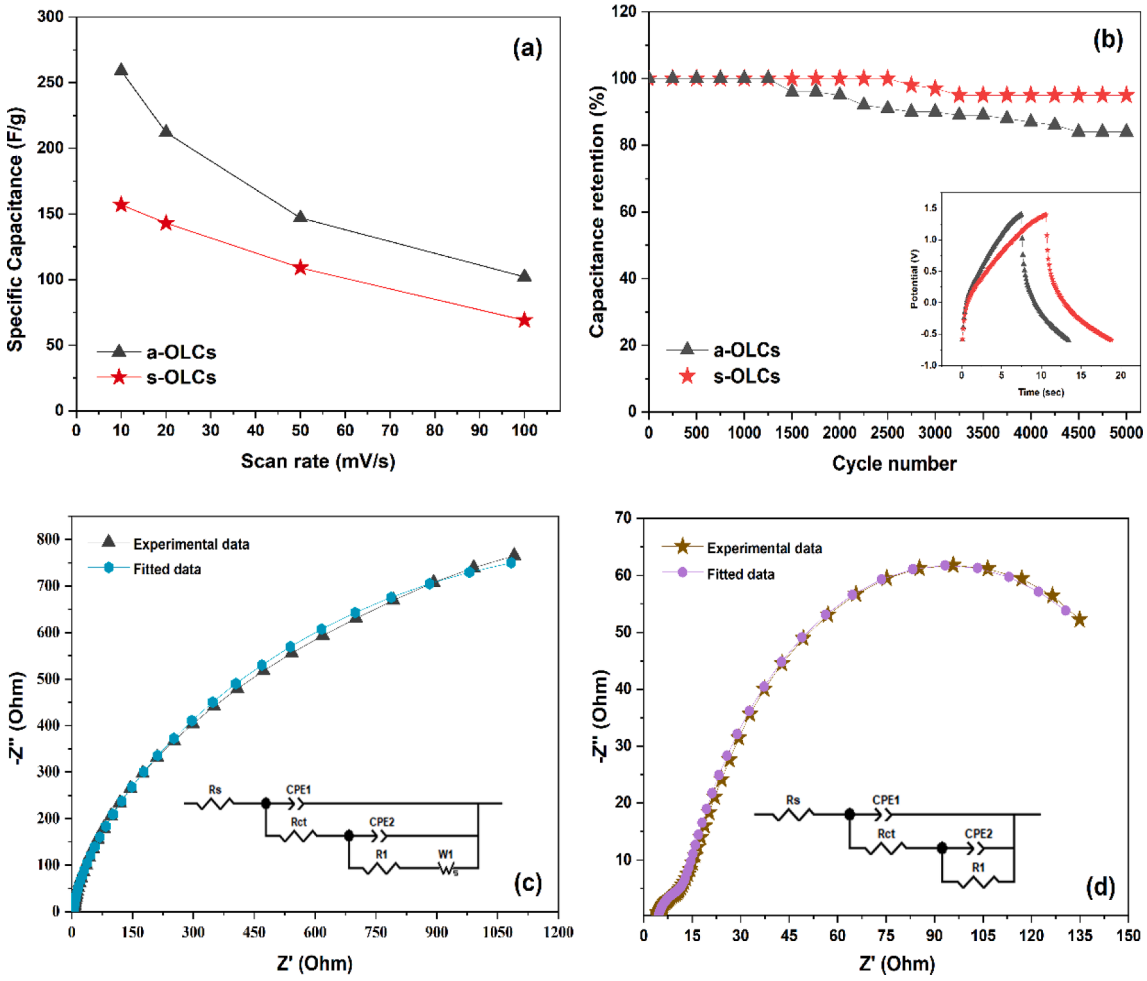

Fig. 9. (a) Specific capacitance at varying scan rates, (b) Cyclic performance of as-synthesized and sonicated OLCs at a current density of 5 A/g (inset: GCD curve at 5 A/g), Nyquist plots of (c) as-synthesized OLCs and (d) sonicated OLCs electrodes (Insets: Equivalent circuit).

material's structure and surface functional groups in ion transition and diffusion.

Table S2 summarizes the published reports on the electrochemical performances of onion-like carbon structures in a 3-electrode cell configuration. As can be observed, the performance of the samples in the present study is considerably superior to that of activated, ozonized, and composite OLCs. With an objective to improve the energy storage ability of the synthesized OLCs by providing meaningful insight on the influence of critical parameters of sonication, including the solvent type, time, and temperature on the supercapacitive performance of the a-OLCs, these conditions were explored and optimized.

3.3. Influence of sonochemical parameters on the electrochemical behavior

It has previously been demonstrated that ultrasonic treatment of carbon nanomaterials with different solvents significantly affects their electrochemical performance. Solvents with high vapor pressure, density, viscosity, or surface tension inhibit cavitation, hindering sonochemical reactions and oxidation of the surface of the active material [51]. This alters the textural and surface chemical properties of the active material, affecting their supercapacitive performance.

To investigate the effect of solvent on the capacitive performance of a-OLCs, they were dispersed in a variety of solvents, including acetonitrile, DMF, DMSO, ethanol, H_2O_2, and NMP. These highly stable suspensions were sonicated at 60 °C for 30 min. Fig. 10(a) depicts the CV plot for a-OLCs sonicated in various solvents. The electrochemical response of sonicated a-OLCs in the chosen solvents is significantly improved over that of the unsonicated OLCs. While the selected solvents enhance the relative supercapacitive characteristics, a-OLCs sonicated in DMF exhibit the best capacitive behavior, with a specific capacitance of 182 F/g (100 mV/s), indicating excellent ion accessibility to the surface and rapid current response. Additionally, the CV curves of a-OLCs dispersed in DMF without sonication (refer to the inset of Fig. 10(a)) are examined to determine whether the solvent or the sonication contribute to the high specific capacitance of the OLCs. It is observed that without being sonicated, the a-OLCs show a specific capacitance of 77 F/g. This finding further establishes the importance of sonication in enhancing the energy storage capabilities of the active material. Also, when DMF is used as the solvent, the CV curves exhibit a quasi-rectangular geometry typical of EDLC.

The reason for enhancement in the specific capacitance is that, upon sonication of a-OLCs in DMF, while the unstable oxygen-containing groups are gently removed, the reaction between $–NH_2$ (from methylamine) and –COOH (from a-OLCs) form amide bonds and thus introduce N–H groups onto the a-OLCs [52]. Partial reduction of oxygen functional groups and formation of N–H groups on the surface of the active material enhances its capacitive performance.

To study the effect of sonication time on the supercapacitive performance of the active material, a-OLCs treated in DMF at 60 °C were sonicated for various durations ranging from 10 to 30 min with a 5-minute interval. As seen in Fig. 10 (b), the current response increases initially but decreases drastically on increasing the sonication time. A specific capacitance of 280 F/g, 298 F/g, 200 F/g, 195 F/g, and 180 F/g

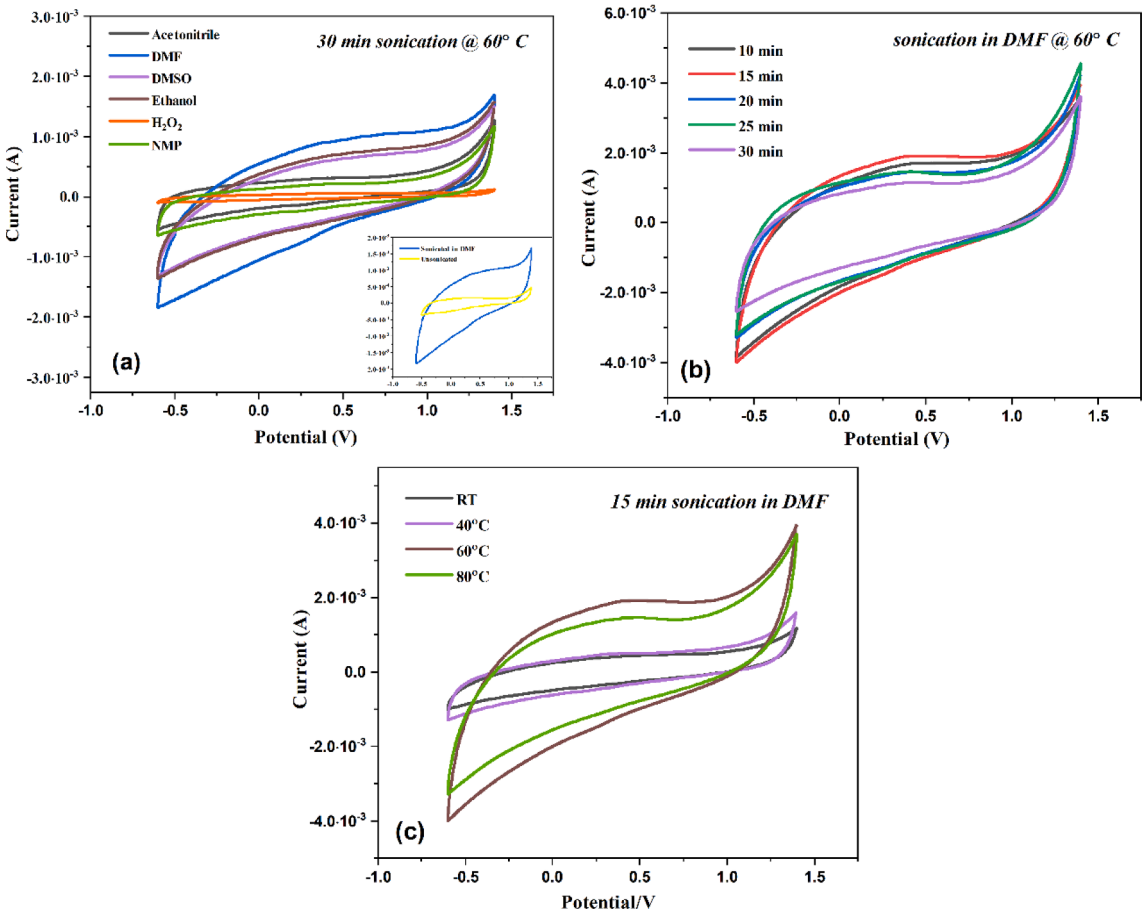

Fig. 10. CV curves of electrodes modified with (a) OLCs sonicated in various solvents, (b) OLCs sonicated in DMF for different durations, and (c) OLCs sonicated in DMF for 15 min at different temperatures.

was obtained for the a-OLCs sonicated for 5, 10, 15, 20, 25, and 30 min, respectively, revealing that the optimum duration for sonication is 15 min. Although sonication can create defects as active sites for storing charges, a longer sonication duration can cause excessive defects on the OLCs, resulting in a large reduction in electrical conductivity [53].

The temperature of the sonicated solution is critical, as the mechanical effects of ultrasound are most effective at temperatures determined by the solvent's physical/chemical properties. [14]. To investigate the same, the electrochemical performance of a-OLCs dispersed in DMF was analyzed after 15 min of sonication at RT, 40 °C, 60 °C, and 80 °C (Fig. 10 (c)). Notably, 60 °C was the optimum temperature for the best performance of the a-OLCs dispersed in DMF, with a relatively high specific capacitance of 300 F/g. Since heating creates defects for charge accumulation and charge generation provides a greater driving force for transfer, the charge-transfer resistance of a-OLCs decreases when heated. However, too many defects reduce the active material's electrical conductivity, resulting in larger charge transfer resistance [54]. The smallest charge transfer resistance, in this case, is consistent with its largest current response and higher capacitance values.

Table 1 illustrates the influence of the solvent, duration of sonication, and the sonication temperature on the specific capacitance of the active material. It is observed that sonication of a-OLCs in DMF at 60 °C for 15 min results in the best energy storage characteristics (a-OLCs treated in this manner would hereafter be referred to as o-OLCs). These findings emphasize the significance of optimizing the key sonication parameters for the best supercapacitive performance of the active material. The enhancement in the capacitance value brought about by sonication could be attributed to the tuning of electrochemical attributes

Table 1
Variation in the specific capacitance of OLCs at 100 mV/s for different sonication conditions.

Sonication Parameters	Specific capacitance at different sonication conditions					
Solvent **(30 min, 60 °C)**	**Acetonitrile**	**DMF**	**DMSO**	**Ethanol**	**H_2O_2**	**NMP**
	97 F/g	182 F/g	125 F/g	140 F/g	42 F/g	85 F/g
Time **(DMF, 60 °C)**	**10 min**	**15 min**	**20 min**	**25 min**	**30 min**	
	280 F/g	298 F/g	200 F/g	195 F/g	180 F/g	
Temperature **(DMF, 15 min)**	**RT**	**40 °C**	**60 °C**	**80 °C**		
	80 F/g	100 F/g	300 F/g	230 F/g		

like ion or charge storage and accelerated surface reactions, beneficial for the capacitive behavior.

Fig. 11(a) shows the CV curves of o-OLCs measured at different scan rates. The similar shapes of the CV curves at different scan rates suggest the high electrochemical reversibility and the remarkable EDLC behavior of the o-OLCs. Fig. 11(b) depicts the specific capacitance of the active material as a function of scan rate. The o-OLCs show a maximum specific capacitance of 647 F/g at 10 A/g with almost a 3-fold increase in the capacitance values compared to a-OLCs (259 F/g). It is also observed from the 5000 charge-discharge processes for the optimized electrode material portrayed in Fig. 11(c) that the capacitance retention is 97%,

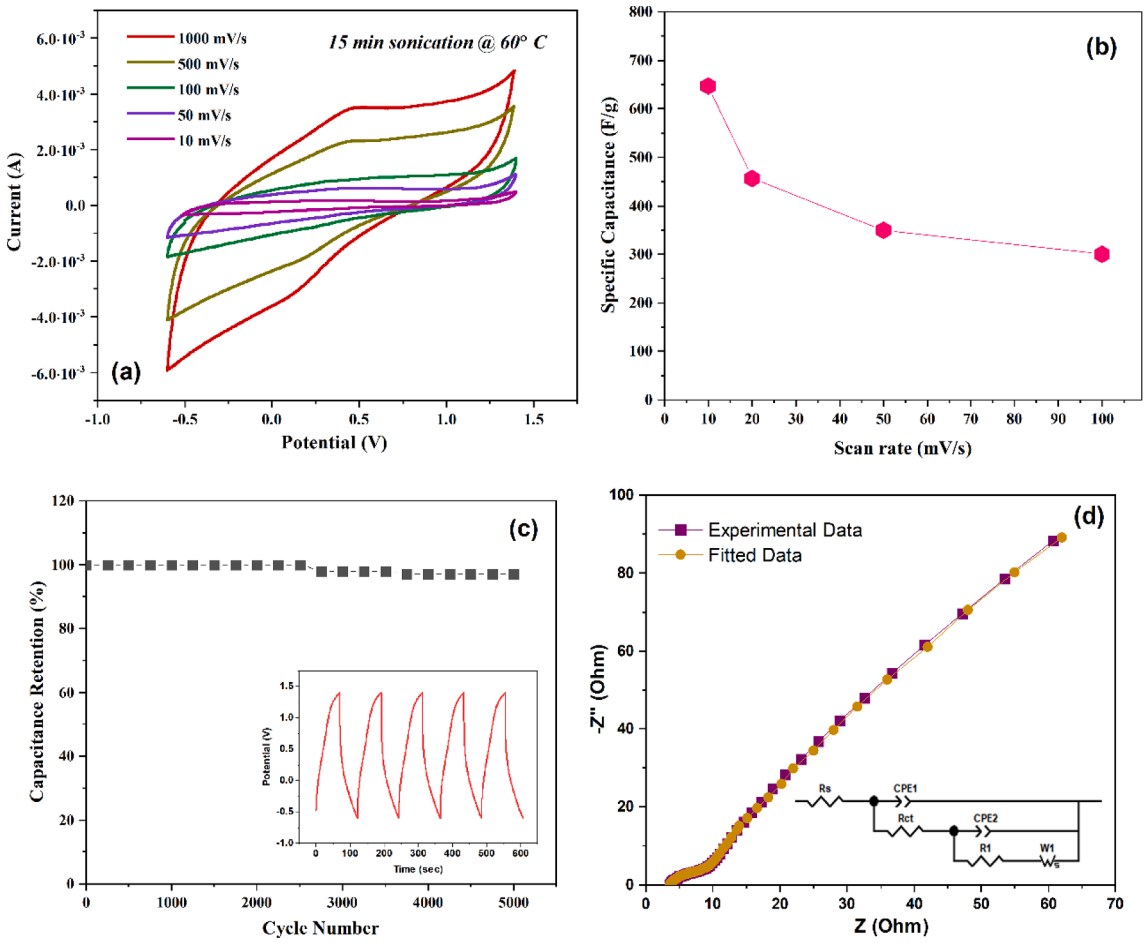

Fig. 11. (a) CV curves at different scan rates, (b) Specific capacitance at varying scan rates, and (c) Cyclic performance at a current density of 5 A/g (Inset: GCD curve at 5 A/g), and (d) Nyquist plots of as-synthesized o-OLCs.

and there is only a 3% loss of initial capacitance. The inset shows the symmetrical GCD curve of o-OLCs at 5 A/g. In the Nyquist plots of the o-OLCs demonstrated in Fig. 11(d), the geometry of the curve at the low-frequency region indicates its excellent capacitive behavior. The electrolyte resistance, R_s, and obtained charge-transfer resistance, R_{ct}, are calculated to be 4 Ω and 3 Ω, respectively. These results suggest that the optimized OLCs electrode possesses a suitable density of defects to induce high charge accumulation and maintain high electrical conductivity simultaneously.

In a nutshell, the best energy storage ability is obtained for the o-OLCs sonicated in DMF at 60 °C for 15 min. This work successfully applies simple heating-assisted sonication in a suitable solvent for an optimum duration to vastly improve the energy storage ability of the OLCs modified electrode. We suggest that future studies which employ OLCs as an active material for electrochemical applications could utilize DMF as the suitable solvent for sonication.

3.4. Electrochemical quantification of methylene blue by the o-OLCs sensor

The high dispersibility, binder-free adhesion, excellent mechanical stability, and superior electrochemical activity, including the efficient charge-transfer capability of the electroactive o-OLCs, could be exploited for electro-analytical applications as well. Experimental investigations for the application of pristine OLCs as an electrochemical sensor are sparse. OLCs-based electrochemical sensors reported so far are either in the form of OLCs-polymer composites, OLCs-metal/metal oxide composites, or heteroatom-doped OLCs. Additionally, the surface of OLCs employed for electrochemical detection is generally modified by surfactants or conducting polymers [55–58]. In this context, considering the simplicity, time, cost, and green chemistry for the fabrication of sensors, the current study is further advanced in demonstrating the applicability of o-OLCs by utilizing it for electrochemical quantification of MB at the picomolar level.

The analytical electrochemical performance of o-OLCs was studied at various concentrations of MB under the optimal experimental conditions using the square wave voltammetry (SWV) technique. The voltammograms recorded for o-OLCs modified GCE in 0.1 M HCl are presented in Fig. 12 (a). The characteristic oxidation peak of MB is generally observed between −0.1 to −0.4 V, depending upon the pH of the electrolyte used [59]. In the present study, the oxidation peak of MB is observed at ~−0.01 V, which increases with an increase in the concentration of MB without affecting the oxidation potential in the range of 100 pM to 1000 pM. The calibration plot of the MB concentration and its corresponding peak current is depicted in Fig. 12(b). An excellent linear dependence is observed in the range of 100–1000 pM with a regression equation of I_P (μA) = 0.0325C (pM) + 0.5460 and R^2 value of 0.999. The calculated limit of detection (LOD) is 64.23 pM, which signifies the superior performance of the designed sensor. The analytical merit of the present sensor is compared to those reported previously in the literature in Table S3. As can be seen from the table, none of the listed sensors could achieve a linear working range and LOD as low as those accomplished in this study, which indicates the excellent electron transfer kinetics between the o-OLCs sensor and MB and thus the sensor's practicality in applications requiring ultrasensitive detection.

Since anti-interference is a crucial component in electrochemical

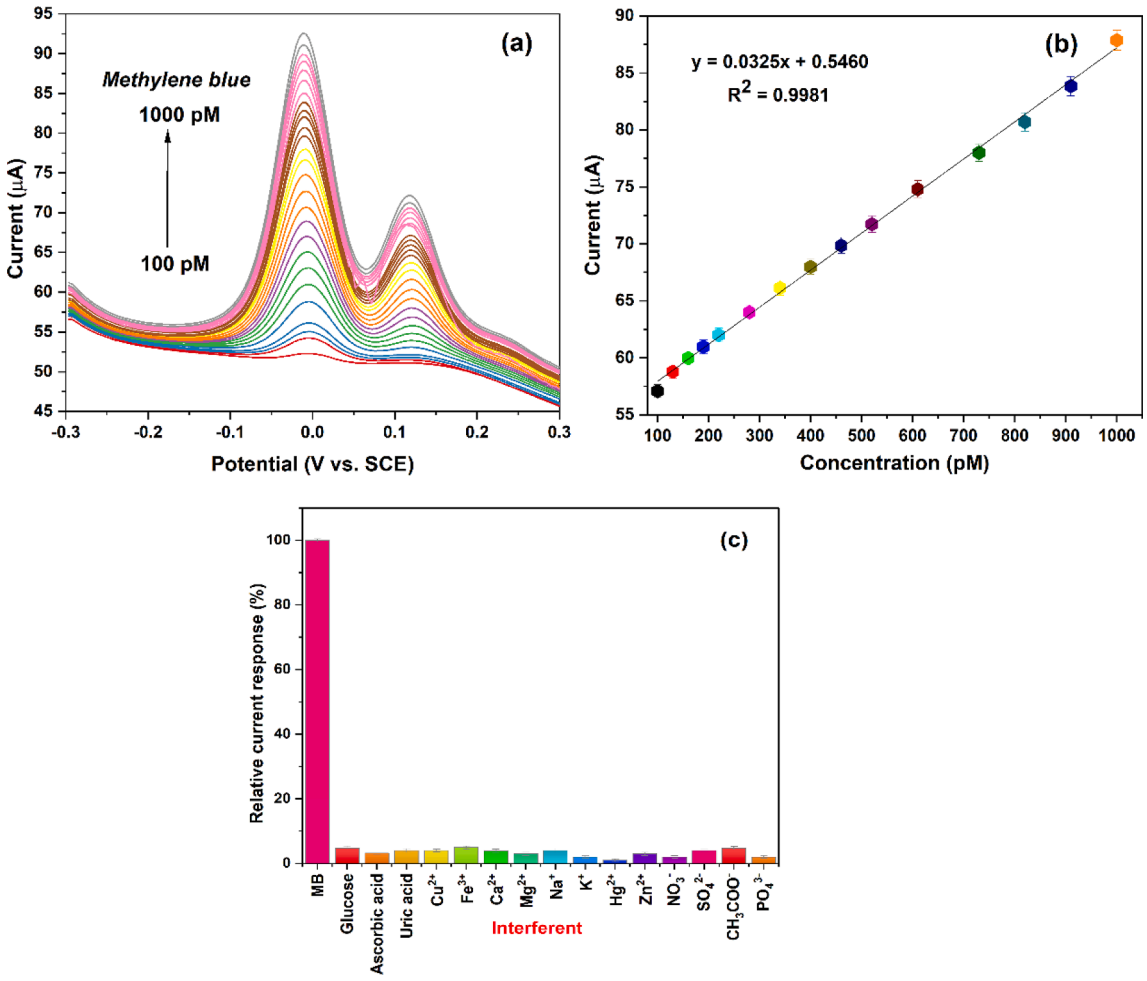

Fig. 12. (a) Square wave voltammetric response of o-OLCs modified GCE for determination of MB, (b) Calibration plot of concentration of MB vs. peak current, and (c) selectivity studies in the presence of some common interfering species.

sensing, the effect of interference by various possible interfering agents was investigated to determine the selectivity of the o-OLCs sensor. Fig. 12(c) depicts the interference effect of different cations and anions on the current signal of MB, using the developed sensor. According to the bar graph, the studied interferents have either minimal or negligible interference on the peak current of MB (RSD < 5%). In other words, the fabricated sensor is highly selective for assessing MB in actual samples containing other ions. Aside from its high selectivity, sensitivity, and reproducibility, the o-OLCs sensor is cost-effective because it could detect MB in multiple samples by simply rinsing with deionized water between analyses.

Having established the high sensitivity and selectivity of the developed sensor, it is crucial to determine its versatility and reliability. Therefore, the o-OLCs sensor was applied to detect three different concentrations (300 pM, 600 pM, and 900 pM) of MB prepared from its pharmaceutical formulation (MB injection USP, 10 mg/mL, Blueject ®, Vulcan Laboratories Pvt. Ltd, India). Although spiking a known concentration of MB, the oxidation peak current of MB was found to increase linearly without any shift in the peak potential. The concentration of MB was determined at the o-OLCs modified electrode using the standard addition method. Each addition was measured thrice using the SWV technique under the optimal working conditions. The obtained results are tabulated in Table 2. The recovery profile shows that the % recovery ranges between 99.4% and 101.2%, and the RSD is below 3%. This demonstrates that the developed sensor is highly accurate at detecting MB in real-world samples, indicating a promising analytical sensing platform for pharmaceuticals containing MB.

Table 2
Recovery profile of MB in its pharmaceutical formulation.

Sample	Added (pM)	Found (pM)	Recovery (%)	RSD (%)
MB injection (10 mg/mL)	300	303.54	101.19	2.86
	600	596.17	99.36	1.73
	900	901.45	100.16	1.32

4. Conclusion

To summarize, mesoporous OLCs were successfully produced using a simple and scalable synthesis approach from a hydrocarbon precursor, paraffin oil, and the as-prepared OLCs were sonochemically tailored for optimal supercapacitive performance. This study demonstrates that the judicious fabrication of active electrode material is critical, as the sonochemical parameters can significantly impact the supercapacitive behavior. Under optimized conditions, the OLCs exhibit a specific capacitance of 647 F/g, excellent cyclic performance over 5000 charge/discharge cycles with a retention of 97% of initial specific capacitance, and a significantly low charge transfer resistance of 3 Ω, showcasing its potential applicability as an active electrode material in electrochemical energy storage. The OLCs also portray outstanding electrochemical sensing parameters with a wide linear range of 100–1000 pM, an ultralow limit of detection of 64.23 pM, and high selectivity, as well as excellent reproducibility, high stability, and satisfactory recovery for quantification of MB, a potential COVID-19 drug. This study

demonstrates that the developed simple and low-cost OLCs sensor could be successfully applied in clinical analysis and quality control of MB, the possible virus warrior, with high accuracy and reliability, thereby directly benefiting the pharmaceutical industry and indirectly saving the lives of several critically ill COVID-19 patients.

5. Patent

This work is a part of a patent application filed with the Indian Patent Office.

Details: A. V. Ramya and Manoj. B, CHRIST (Deemed to be University), Indian Patent No. E-101/8801/2020-CHE, Application No. 202,041,033,633 A, Published on 21st August 2020.

Funding

This research did not receive any specific grant from funding agencies in the public, commercial, or not-for-profit sectors.

CRediT authorship contribution statement

Athiyanam Venkatesan Ramya: Conceptualization, Methodology, Formal analysis, Investigation, Data curation, Writing - original draft, Visualization. **Riya Thomas:** Data curation, Investigation, Methodology. **Manoj Balachandran:** Validation, Resources, Writing - review & editing, Supervision, Project administration.

Declaration of Competing Interest

The authors declare that they have no known competing financial interests or personal relationships that could have appeared to influence the work reported in this paper.

Acknowledgments

The authors thank the Centre for Research, CHRIST (Deemed to be University), Bengaluru, India, for providing the necessary facilities to complete this study successfully. A.V. Ramya and Riya Thomas are thankful to DST for their fellowship grants DST/INSPIRE/03/2015/004970 and DST/INSPIRE/03/2018/002742, respectively. We also acknowledge CeNSE IISc (Bengaluru), IUCNN MG University (Kerala), and SAIF CUSAT (Kerala) for the characterization facilities.

Appendix A. Supplementary data

Supplementary data to this article can be found online at https://doi.org/10.1016/j.ultsonch.2021.105767.

References

[1] S. Balasubramaniam, A. Mohanty, S.K. Balasingam, S.J. Kim, A. Ramadoss, Comprehensive insight into the mechanism, material selection and performance evaluation of supercapatteries, Nano-Micro Lett. 12 (2020) 85, https://doi.org/10.1007/s40820-020-0413-7.

[2] D. Mohapatra, S. Badrayyana, S. Parida, A facile method for high yield synthesis of carbon nano onions for designing binder-free flexible supercapacitor, AIP Conf. Proc. 2017 (1832) 1–4, https://doi.org/10.1063/1.4980302.

[3] Y. Gao, Y.S. Zhou, M. Qian, X.N. He, J. Redepenning, P. Goodman, H.M. Li, L. Jiang, Y.F. Lu, Chemical activation of carbon nano-onions for high-rate supercapacitor electrodes, Carbon N. Y. 51 (2013) 52–58, https://doi.org/10.1016/j.carbon.2012.08.009.

[4] R. Borgohain, J. Yang, J.P. Selegue, D.Y. Kim, Controlled synthesis, efficient purification, and electrochemical characterization of arc-discharge carbon nano-onions, Carbon N. Y. 66 (2014) 272–284, https://doi.org/10.1016/j.carbon.2013.09.001.

[5] C. Portet, G. Yushin, Y. Gogotsi, Electrochemical performance of carbon onions, nanodiamonds, carbon black and multiwalled nanotubes in electrical double layer capacitors, Carbon N. Y. 45 (13) (2007) 2511–2518, https://doi.org/10.1016/j.carbon.2007.08.024.

[6] N. Jäckel, D. Weingarth, M. Zeiger, M. Aslan, I. Grobelsek, V. Presser, Comparison of carbon onions and carbon blacks as conductive additives for carbon supercapacitors in organic electrolytes, J. Power Sources 272 (2014) 1122–1133, https://doi.org/10.1016/j.jpowsour.2014.08.090.

[7] R. Berenguer Betrián, Trends and research challenges in supercapacitors, (2015) 9–13.

[8] D. Hulicova-Jurcakova, M. Seredych, G.Q. Lu, T.J. Bandosz, Combined effect of nitrogen- and oxygen-containing functional groups of microporous activated carbon on its electrochemical performance in supercapacitors, Adv. Funct. Mater. 19 (3) (2009) 438–447, https://doi.org/10.1002/adfm.v19:310.1002/adfm.200801236.

[9] D. Rosenthal, M. Ruta, R. Schlögl, L. Kiwi-Minsker, Combined XPS and TPD study of oxygen-functionalized carbon nanofibers grown on sintered metal fibers, Carbon N. Y. 48 (6) (2010) 1835–1843, https://doi.org/10.1016/j.carbon.2010.01.029.

[10] O. Mykhailiv, A. Lapinski, A. Molina-Ontoria, E. Regulska, L. Echegoyen, A. T. Dubis, M.E. Plonska-Brzezinska, Influence of the synthetic conditions on the structural and electrochemical properties of carbon nano-onions, ChemPhysChem 16 (10) (2015) 2182–2191, https://doi.org/10.1002/cphc.201500061.

[11] O. Butsyk, P. Olejnik, E. Romero, M.E. Plonska-Brzezinska, Postsynthetic treatment of carbon nano-onions: Surface modification by heteroatoms to enhance their capacitive and electrocatalytic properties, Carbon N. Y. 147 (2019) 90–104, https://doi.org/10.1016/j.carbon.2019.02.063.

[12] Y. Yang, J. Zhang, J. Zhuang, X. Wang, Synthesis of nitrogen-doped carbon nanostructures from polyurethane sponge for bioimaging and catalysis, Nanoscale. 7 (29) (2015) 12284–12290, https://doi.org/10.1039/C5NR03481G.

[13] K. Chatterjee, M. Ashokkumar, H. Gullapalli, Y. Gong, R. Vajtai, P. Thanikaivelan, P.M. Ajayan, Nitrogen-rich carbon nano-onions for oxygen reduction reaction, Carbon N. Y. 130 (2018) 645–651, https://doi.org/10.1016/j.carbon.2018.01.052.

[14] C.U. Okoli, K.A. Kuttiyiel, J. Cole, J. McCutchen, H. Tawfik, R.R. Adzic, D. Mahajan, Solvent effect in sonochemical synthesis of metal-alloy nanoparticles for use as electrocatalysts, Ultrason. Sonochem. 41 (2018) 427–434, https://doi.org/10.1016/j.ultsonch.2017.09.049.

[15] N. Dabholkar, S. Gorantla, S.K. Dubey, A. Alexander, R. Taliyan, G. Singhvi, Repurposing methylene blue in the management of COVID-19: Mechanistic aspects and clinical investigations, Biomed. Pharmacother. 142 (2021) 112023, https://doi.org/10.1016/j.biopha.2021.112023.

[16] D. Bojadzic, O. Alcazar, P. Buchwald, Methylene blue inhibits the SARS-CoV-2 spike–ACE2 protein-protein interaction – a mechanism that can contribute to its antiviral activity against COVID-19, Front. Pharmacol. 11 (2021) 1–9, https://doi.org/10.3389/fphar.2020.600372.

[17] D. Hamidi-Alamdari, S. Hafizi-Lotfabadi, A. Bagheri-Moghaddam, H. Safari, M. Mozdourian, Z. Javidarabshahi, A. Peivandi-Yazdi, A. Ali-Zeraati, A. Sedaghat, F. Poursadegh, F. Barazandeh-Ahmadabadi, M. Agheli-Rad, S.M. Tavousi, S. Vojouhi, S. Amini, M. Amini, S. Majid-Hosseini, A. Tavanaee-Sani, A. Ghiabi, S. Nabavi-Mahalli, N. Morovatdar, O. Rajabi, G. Koliakos, Methylene blue for treatment of hospitalized covid-19 patients: a randomized, controlled, open-label clinical trial, phase 2, Rev. Invest. Clin. 73 (2021) 190–198, https://doi.org/10.24875/RIC.21000028.

[18] S. Mennickent, M. de Diego, Analytical Method Validation as the First Step in Drug Quality Control, in: Qual. Manag. Qual. Control - New Trends Dev., IntechOpen, 2019: pp. 1–21. https://doi.org/10.5772/intechopen.82826.

[19] M.A. Mohamed, N.S. Abdelwahab, C.E. Banks, Electroanalytical sensing of the antimicrobial drug linezolid utilising an electrochemical sensing platform based upon a multiwalled carbon nanotubes/bromocresol green modified carbon paste electrode, Anal. Methods 8 (22) (2016) 4345–4353, https://doi.org/10.1039/C6AY00454G.

[20] R. Bajpai, L. Rapoport, K. Amsalem, H.D. Wagner, Rapid growth of onion-like carbon nanospheres in a microwave oven, CrystEngComm 18 (2) (2016) 230–239, https://doi.org/10.1039/C5CE01785H.

[21] M. Zeiger, N. Jäckel, V.N. Mochalin, V. Presser, Review: carbon onions for electrochemical energy storage, J. Mater. Chem. A 4 (9) (2016) 3172–3196, https://doi.org/10.1039/C5TA08295A.

[22] B.P. Dhonge, D.E. Motaung, C.P. Liu, Y.C. Li, B.W. Mwakikunga, Nano-scale carbon onions produced by laser photolysis of toluene for detection of optical, humidity, acetone, methanol and ethanol stimuli, Sens. Actuators B Chem. 215 (2015) 30–38, https://doi.org/10.1016/j.snb.2015.03.033.

[23] R.A. Venkatesan, M. Balachandran, Novel carbon nano-onions from paraffinum liquidum for rapid and efficient removal of industrial dye from wastewater, Environ. Sci. Pollut. Res. 27 (35) (2020) 43845–43864, https://doi.org/10.1007/s11356-020-09981-w.

[24] T. Skaltsas, X. Ke, C. Bittencourt, N. Tagmatarchis, Ultrasonication induces oxygenated species and defects onto exfoliated graphene, J. Phys. Chem. C 117 (44) (2013) 23272–23278, https://doi.org/10.1021/jp4057048.

[25] G.T.T. Le, N. Chanlek, J. Manyam, P. Opaprakasit, N. Grisdanurak, P. Sreearunothai, Insight into the ultrasonication of graphene oxide with strong changes in its properties and performance for adsorption applications, Chem. Eng. J. 373 (2019) 1212–1222, https://doi.org/10.1016/j.cej.2019.05.108.

[26] R. Krishnan, J. John, B. Manoj, Raman spectroscopy investigation of camphor Soot: spectral analysis and structural information, Int. J. Electrochem. Sci. 8 (2013) 9421–9428.

[27] A.V. Ramya, M. Balachandran, Valorization of agro-industrial fruit peel waste to fluorescent nanocarbon sensor: ultrasensitive detection of potentially hazardous tropane alkaloid, Front. Environ. Sci. Eng. 16 (2021) 1–11, https://doi.org/10.1007/s11783-021-1461-z.

[28] H.A. Calderon, A. Okonkwo, I. Estrada-Guel, V.G. Hadjiev, F. Alvarez-Ramírez, F. C. Robles Hernández, HRTEM low dose: the unfold of the morphed graphene, from amorphous carbon to morphed graphenes, Adv. Struct. Chem. Imaging. 2 (1) (2016), https://doi.org/10.1186/s40679-016-0024-z.

[29] A. Mohan, A.V. Ramya, B. Manoj, Synthesis and characterization of sp 2 - sp 3 bonded disordered graphene like nanocarbon from coconut shell, Adv. Sci. Eng. Med. 8 (2) (2016) 112–116, https://doi.org/10.1166/asem.2016.1840.
[30] A.V. Ramya, A.N. Mohan, B. Manoj, Wrinkled graphene: Synthesis and characterization of few layer graphene-like nanocarbons from kerosene, Mater. Sci. Pol. 34 (2016) 330–336, https://doi.org/10.1515/msp-2016-0061.
[31] D. López-Díaz, M. López Holgado, J.L. García-Fierro, M.M. Velázquez, Evolution of the Raman spectrum with the chemical composition of graphene oxide, J. Phys. Chem. C 121 (37) (2017) 20489–20497, https://doi.org/10.1021/acs.jpcc.7b06236.
[32] W. Sun, X. Zhang, H.-R. Jia, Y.-X. Zhu, Y. Guo, G.e. Gao, Y.-H. Li, F.-G. Wu, Water-dispersible candle soot-derived carbon nano-onion clusters for imaging-guided photothermal cancer therapy, Small 15 (11) (2019) 1804575, https://doi.org/10.1002/smll.201804575.
[33] R. Thomas, E. Jayaseeli, N.M.S. Sharma, B. Manoj, Opto-electric property relationship in phosphorus embedded nanocarbon, Results Phys. 10 (2018) 633–639, https://doi.org/10.1016/j.rinp.2018.07.018.
[34] S. Shanmugapriya, S. Surendran, Y.S. Lee, R.K. Selvan, Improved surface charge storage properties of Prosopis juliflora (pods) derived onion–like porous carbon through redox-mediated reactions for electric double layer capacitors, Appl. Surf. Sci. 492 (2019) 896–908, https://doi.org/10.1016/j.apsusc.2019.06.147.
[35] O.C. Compton, Z. An, K.W. Putz, B.J. Hong, B.G. Hauser, L. Catherine Brinson, S. T. Nguyen, Additive-free hydrogelation of graphene oxide by ultrasonication, Carbon N. Y. 50 (10) (2012) 3399–3406, https://doi.org/10.1016/j.carbon.2012.01.061.
[36] T. Das, P.K. Boruah, M.R. Das, B.K. Saikia, Formation of onion-like fullerene and chemically converted graphene-like nanosheets from low-quality coals: application in photocatalytic degradation of 2-nitrophenol, RSC Adv. 6 (42) (2016) 35177–35190, https://doi.org/10.1039/C6RA04392E.
[37] Y.J. Oh, J.J. Yoo, Y. Il Kim, J.K. Yoon, H.N. Yoon, J.H. Kim, S. Bin Park, Oxygen functional groups and electrochemical capacitive behavior of incompletely reduced graphene oxides as a thin-film electrode of supercapacitor, Electrochim. Acta 116 (2014) 118–128, https://doi.org/10.1016/j.electacta.2013.11.040.
[38] S.W. Nam, C. Jung, H. Li, M. Yu, J.R.V. Flora, L.K. Boateng, N. Her, K.D. Zoh, Y. Yoon, Adsorption characteristics of diclofenac and sulfamethoxazole to graphene oxide in aqueous solution, Chemosphere 136 (2015) 20–26, https://doi.org/10.1016/j.chemosphere.2015.03.061.
[39] G. Gonçalves, M. Vila, I. Bdikin, A. De Andrés, N. Emami, R.A.S. Ferreira, L. D. Carlos, J. Grácio, P.A.A.P. Marques, Breakdown into nanoscale of graphene oxide: confined hot spot atomic reduction and fragmentation, Sci. Rep. 4 (2014) 1–8, https://doi.org/10.1038/srep06735.
[40] D. Lozano-Castelló, J.M. Calo, D. Cazorla-Amorós, A. Linares-Solano, Carbon activation with KOH as explored by temperature programmed techniques, and the effects of hydrogen, Carbon N. Y. 45 (13) (2007) 2529–2536, https://doi.org/10.1016/j.carbon.2007.08.021.
[41] D. Mohapatra, S. Badrayyana, S. Parida, Designing binder-free, flexible electrodes for high-performance supercapacitors based on pristine carbon nano-onions and their composite with CuO nanoparticles, RSC Adv. 6 (18) (2016) 14720–14729, https://doi.org/10.1039/C5RA23700A.
[42] C.-T. Hsieh, H. Teng, Influence of oxygen treatment on electric double-layer capacitance of activated carbon fabrics, Carbon N. Y. 40 (5) (2002) 667–674, https://doi.org/10.1016/S0008-6223(01)00182-8.
[43] N. Lei, P. Li, W. Xue, J. Xu, Simple graphene chemiresistors as pH sensors: Fabrication and characterization, Meas. Sci. Technol. 22 (10) (2011) 107002, https://doi.org/10.1088/0957-0233/22/10/107002.
[44] R. Thomas, M. Balachandran, Luminescence and energy storage characteristics of coke-based graphite oxide, Mater. Chem. Phys. 257 (2021) 123854, https://doi.org/10.1016/j.matchemphys.2020.123854.
[45] M. Zhu, J. Lan, X. Zhang, G. Sui, X. Yang, Porous carbon derived from Ailanthus altissima with unique honeycomb-like microstructure for high-performance supercapacitors, New J. Chem. 41 (11) (2017) 4281–4285, https://doi.org/10.1039/C7NJ01127J.
[46] H. Cao, X. Peng, M. Zhao, P. Liu, B. Xu, J. Guo, Oxygen functional groups improve the energy storage performances of graphene electrochemical supercapacitors, RSC Adv. 8 (6) (2018) 2858–2865, https://doi.org/10.1039/C7RA12425B.
[47] W. Yang, Y. Li, Y. Feng, High electrochemical performance from oxygen functional groups containing porous activated carbon electrode of supercapacitors, Materials (Basel) 11 (2018) 2455, https://doi.org/10.3390/ma11122455.
[48] W. Zhang, J. Wang, L. Bao, Z. Gao, J. Yu, Nanopores created by carbon onion conductive agent providing enhanced capacitance in supercapacitors, Diam. Relat. Mater. 96 (2019) 231–236, https://doi.org/10.1016/j.diamond.2019.05.015.
[49] J.D. Velásquez, M. Tomczykowa, M.E. Plonska-Brzezinska, M.N. Chaur, Evaluation of the covalent functionalization of carbon nano-onions with pyrene moieties for supercapacitor applications, Materials (Basel) 13 (2020) 1141, https://doi.org/10.3390/ma13051141.
[50] Y. He, Y. Zhang, X. Li, Z. Lv, X. Wang, Z. Liu, X. Huang, Capacitive mechanism of oxygen functional groups on carbon surface in supercapacitors, Electrochim. Acta 282 (2018) 618–625, https://doi.org/10.1016/j.electacta.2018.06.103.
[51] B. Lo, E. Gorczyca, S. Kasapis, B. Zisu, Effect of low-frequency ultrasound on the particle size, solubility and surface charge of reconstituted sodium caseinate, Ultrason. Sonochem. 58 (2019) 104525, https://doi.org/10.1016/j.ultsonch.2019.03.016.
[52] X.-Z. Tang, N. Srikanth, X.-Q. Feng, C.K. Chua, K. Zhou, Reduced graphene oxide/silver hybrid with N, N-dimethyl formamide for oxygen reduction reactions and surface enhanced Raman scattering, RSC Adv. 6 (104) (2016) 102519–102527, https://doi.org/10.1039/C6RA24322C.
[53] S. Pandey, U.N. Maiti, K. Palanisamy, P. Nikolaev, S. Arepalli, Ultrasonicated double wall carbon nanotubes for enhanced electric double layer capacitance, Appl. Phys. Lett. 104 (23) (2014) 233902, https://doi.org/10.1063/1.4882278.
[54] F. Ali, L. Reinert, J.-M. Levêque, L. Duclaux, F. Muller, S. Saeed, S.S. Shah, Effect of sonication conditions: solvent, time, temperature and reactor type on the preparation of micron sized vermiculite particles, Ultrason. Sonochem. 21 (3) (2014) 1002–1009, https://doi.org/10.1016/j.ultsonch.2013.10.010.
[55] J.P. Bartolome, L. Echegoyen, A. Fragoso, Reactive carbon nano-onion modified glassy carbon surfaces as DNA sensors for human papillomavirus oncogene detection with enhanced sensitivity, Anal. Chem. 87 (13) (2015) 6744–6751, https://doi.org/10.1021/acs.analchem.5b00924.
[56] O.C. Ozoemena, L.J. Shai, T. Maphumulo, K.I. Ozoemena, Electrochemical sensing of dopamine using onion-like carbons and their carbon nanofiber composites, Electrocatalysis 10 (4) (2019) 381–391, https://doi.org/10.1007/s12678-019-00520-x.
[57] V. Singh, Natural source derived carbon nano-onions as electrode material for sensing applications, Diam. Relat. Mater. 87 (2018) 202–207, https://doi.org/10.1016/j.diamond.2018.06.007.
[58] D. Mohapatra, N.S.K. Gowthaman, M.S. Sayed, J.-J. Shim, Simultaneous ultrasensitive determination of dihydroxybenzene isomers using GC electrodes modified with nitrogen-doped carbon nano-onions, Sens. Actuators B Chem. 304 (2020) 127325, https://doi.org/10.1016/j.snb.2019.127325.
[59] H. Ju, J. Zhou, C. Cai, H. Chen, The electrochemical behavior of methylene blue at a microcylinder carbon fiber electrode, Electroanalysis 7 (12) (1995) 1165–1170, https://doi.org/10.1002/elan.1140071213.